Soft Matter

# Emergence and dynamics of unconfined self-organized vortices in active magnetic roller liquids



| | |
|---|---|
| Journal: | *Soft Matter* |
| Manuscript ID | SM-ART-07-2021-001086.R1 |
| Article Type: | Paper |
| Date Submitted by the Author: | 24-Sep-2021 |
| Complete List of Authors: | Han, Koohee; Argonne National Laboratory, Materials Science<br>Glatz, Andreas; Argonne National Laboratory, Materials Science Division<br>Snezhko, Alexey; Argonne National Laboratory, Materials Science Division |
| | |

Soft Matter

ARTICLE TYPE

Cite this: DOI: 00.0000/xxxxxxxxxx

# Emergence and dynamics of unconfined self-organised vortices in active magnetic roller liquids†

Koohee Han,[a,b] Andreas Glatz,[a,c] and Alexey Snezhko*[a]

Received Date
Accepted Date

DOI: 00.0000/xxxxxxxxxx

Actively driven colloids demonstrate complex out-of-equilibrium dynamics often rivaling self-organized patterns and collective behavior observed in living systems. Recent studies revealed the emergence of *steady* macroscopic states with multiple interacting vortices in an unconfined environment that emerge from the coupling between microscale particle rotation and translation. Yet, insights into the microscopic behavior during the vortex emergence, growth, and formation of a multi-vortical state remain lacking. Here, we investigate in experiments and simulations how the microscale magnetic roller behavior leads to the emergence of seed vortices, their aggregation or annihilation, and the formation of stable large-scale vortical structures. We reveal that the coupling of roller-induced hydrodynamic flows guides the local self-densifications and self-organization of the micro-rollers into seed vortices. The resulting multi-vortical state is sensitive to the external magnetic field amplitude and allows tuning the rollers' number density in a vortex and its characteristic size.

## 1 Introduction

Active matter exhibits remarkable collective dynamics over a wide range of length scales[1,2]. Self-organized coherent motion is widespread in Nature, from animal flocks[3,4] to bacterial suspensions[5,6]. Vortex patterns attract special attention in the field of active matter due to their ability to orchestrate coherent rotational motion of large amounts of self-propelled units over substantial distances. Self-organized vortex patterns are common in active matter [7–12], However, in most of the studies the onset of a vortical motion in active colloidal systems typically relies on a confinement realized either by geometrical boundaries or potentials[9,13–17] Although confinement facilitates the spontaneous emergence of vortex structures, it also prescribes the size and location of the emergent vortex. There are a few noticeable exceptions to the above discussion[18–20], where spontaneous formation of dynamic vortices has been promoted through controlling the persistence length of individual self-propelled units realized by either modulation of their activity (run and tumble scenario)[18] or control of the curvature of their trajectories[19].

Active colloids driven by external magnetic fields is a robust platform to explore various emergent collective dynamics and self-organization[21–27]. Recent studies of field-driven active colloids have shown the development of active vortex structures even in unconfined environments[10,18,19,28]. The emergent vortices, comprised of magnetic spinning units acting as macroscopic dynamic entities, have demonstrated the potential for applications in microscale transport either by means of trapping passive particles in the core of the moving vortex[10] or by creating a well controlled macroscopic flow[29].

The discovery of dynamic steady-states with multiple motile vortices formed by magnetic rollers and not defined by a confinement calls for a better understanding of the microscale dynamics related to the spontaneous emergence of self-densifications (vortex precursors), their evolution, and aggregation dynamics that eventually lead to the formation of long-lived macroscopic vortices. The reaction of the system on amplitude changes of the uniaxial magnetic field driving the rolling motion of the particles in the ensemble also requires an investigation.

In this paper, we discuss the underlying processes of vortex emergence and their interaction dynamics in an ensemble of active ferromagnetic rollers driven by a uni-axial alternating current (AC) magnetic field applied perpendicular to the plane of particle motion. We first elucidate how the coupling of roller-induced hydrodynamic flows guides the self-organization of magnetic micro-rollers into an unconfined macroscopic vortex. We further demonstrate that macroscopic hydrodynamic flows induced by an emergent (primary) vortex promotes the formation of neighboring rollers into secondary vortices with opposite chirality. We investigate the role of magnetic repulsive

[a] *Materials Science Division, Argonne National Laboratory, Lemont, IL 60439, USA.* *E-mail: snezhko@anl.gov
[b] *Department of Chemical Engineering, Kyungpook National University, Daegu, Republic of Korea.*
[c] *Department of Physics, Northern Illinois University, DeKalb, IL 60115, USA.*

† Electronic Supplementary Information (ESI) available: [details of any supplementary information available should be included here]. See DOI: 00.0000/00000000.

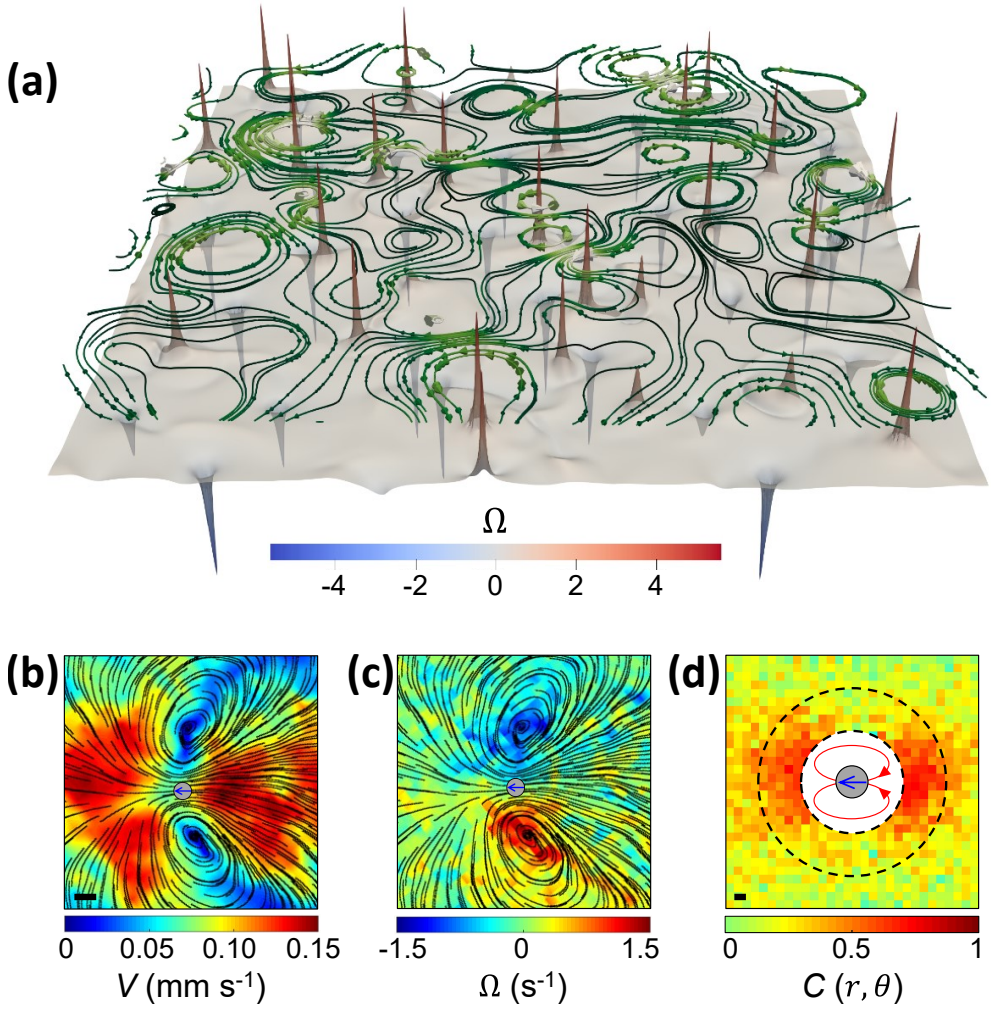


**Fig. 1** Induced hydrodynamic flows of micro-roller colloids. (**a**) Snapshot of a simulated system of size $128 \times 128$ particle diameters in a multi-vortex state showing the vorticity of the particle velocity as iso-surface and the fluid velocity as streamlines (cf. Movies S1 & S2). (**b**) Velocity and (**c**) vorticity field visualization of the roller-induced hydrodynamic flows along with corresponding streamlines. The gray circle indicates the location of the roller generating the hydrodynamic flows where the blue arrow indicates the motion direction of the roller. (**d**) The spatial velocity correlation map of a roller. The ring area between the dashed circles, 200 $\mu$m $< r <$ 400 $\mu$m , contains high velocity correlations guided by the roller-induced hydrodynamic flows shown in (b) and (c). The gray circle indicates the location of the roller where the blue arrow indicates the motion direction of the roller and the red arrows illustrate the direction of the hydrodynamic flows. The scale bars are 0.2 mm.

interactions controlled by the amplitude of the driving magnetic field on characteristics of the emergent multi-vortical state. We reveal that the size and density of the individual vortices could be efficiently manipulated by changing the amplitude of the magnetic field. Our work provides insights into the dynamics of unconfined vortices by taking a close look at the process of vortex emergence and interaction via single-particle tracking, particle image velocimetry (PIV), and simulations based on a continuum model.

## 2 Methods and materials

### 2.1 Experimental system

The studied active magnetic suspension of rollers consists of ferromagnetic nickel (Ni) spheres in water (Alfa Aesar; 125 - 150 $\mu$m) sedimented at the bottom of a flat Petri dish container (Corning; diameter 100 mm, height 15 mm). The magnetic moment per particle is $\mu \approx 0.02 \mu A m^2$. The container was housed on a microscope stage (Leica MZ9.5) where the dynamics of the particles was monitored by means of a fast CMOS camera (iNS1, Integrated Design Tools, Inc.) at a frame rate of 100 frames/s. A uniaxial AC magnetic field is supplied by a pair of custom made precision coils in the Helmholtz configuration to energize the system. The field is applied perpendicular to the bottom surface of the container along the $z$-axis, $H_z = H_0 \sin(2\pi f t)$, where $H_0$ is the field amplitude (30 - 40 G) and $f$ is the field frequency (40 Hz). The energized Ni spheres spontaneously break the uniaxial symmetry of the driving magnetic field and turn into active rollers with no prescribed direction in the $xy$-plane. The underlying mechanism of active rolling motion has been discussed in detail previously[17,30]. In the steady rotation regime ($f$ = 20 - 40 Hz), the Ni spheres rotate synchronously with the external magnetic field, and the friction asymmetry around the spheres

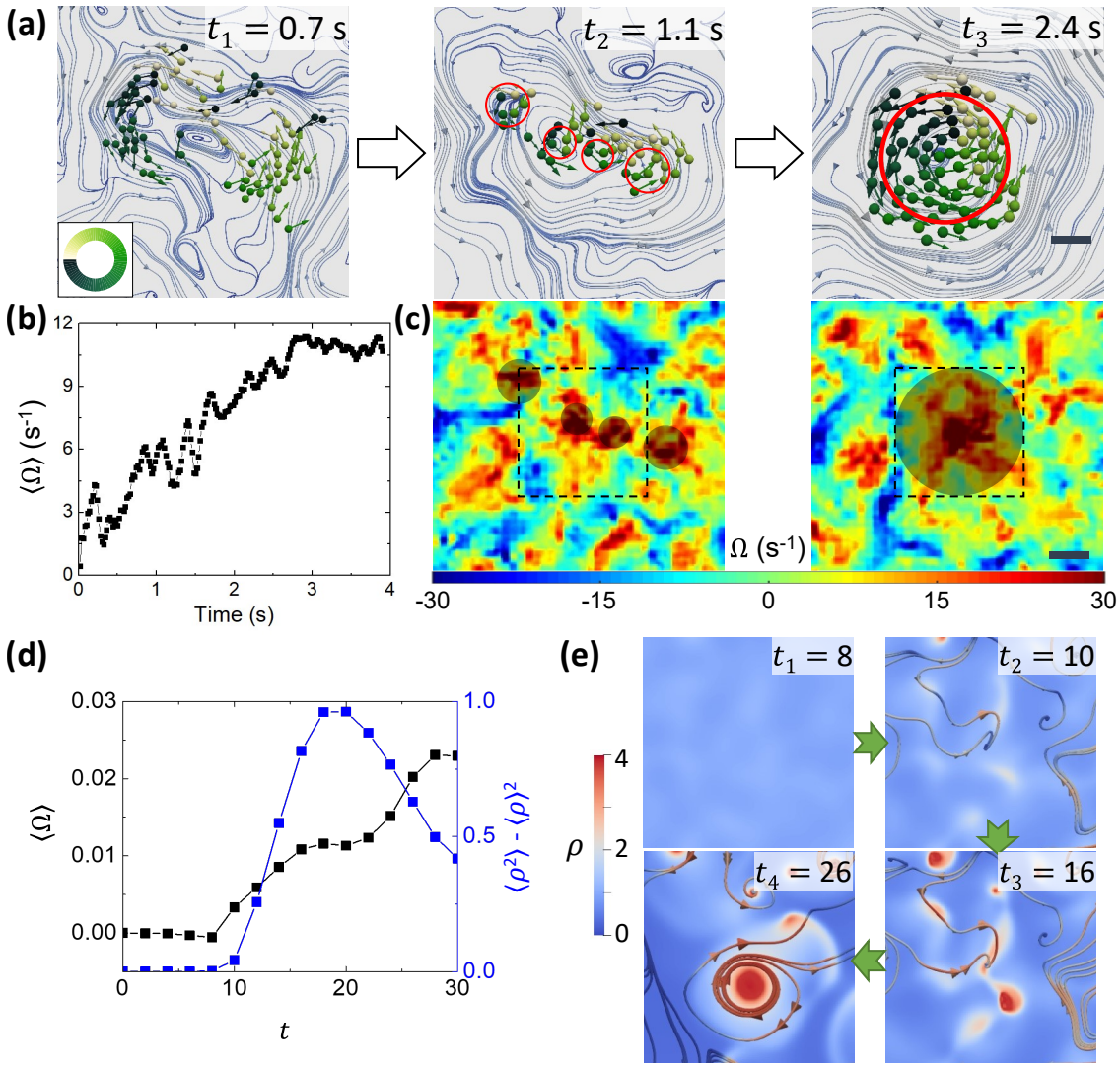


**Fig. 2** Vortex self-emergence dynamics. (**a**) The self-organization process of the rollers visualized by color-coded directions of the roller motion overlaid with the flow streamlines: ($t_1$) multiple flocks, ($t_2$) transient seed vortices, ($t_3$) a stable single vortex. (**b**) The time evolution of the mean vorticity in the area indicated by the dashed line in (c) during the self-organization process. (**c**) The vorticity field of the rollers in the state of transient multiple vortices ($t_2$, left panel) and a stable single-vortex ($t_3$, right panel). The highlighted regions represent the location of the vortices. The scale bars are 1 mm. **(d)** Mean vorticity and variance of the particle density in the region shown in (e) as function of simulation time. **(e)** A region of the simulated system in the initial stage showing the emergence of transient seed vortex states, which later merge into a stable vortex.

rotating in proximity to the solid surface results in a net rolling motion[31,32]. Here, the field frequency controls the rolling speed, and as a result, the activity of the particles. It was previously demonstrated that $f \backsimeq 40$ Hz results in the largest roller-to-roller velocity correlations and leads to an emergence of a macroscopic vortex in a harmonic confinement[17,30].

The multiple vortices observed in the system under investigation are reminiscent of the magnetic colloidal vortices observed in a system of paramagnetic particles actuated by a precessing magnetic field[33]. There, the net torque exerted by the precessing field and multi-body magnetic interactions promote the formation of the spinning clusters (vortices) with a chiral state prescribed by the direction of rotation of the precessing field. In contrast, the vortices formed in ensembles of ferromagnetic rollers actuated by an oscillating single-axis magnetic field spontaneously select their chiral states (clockwise or counter-clockwise)upon emergence, and the hydrodynamic alignment interactions play a pivotal role in dynamic self-densifications and subsequent formation of the roller vortices[28].

### 2.2 Data analysis

To investigate the dynamics of the magnetic rollers, image sequences have been captured and analyzed. Particle tracking was performed by MATLAB scripts based on the Crocker and Grier algorithm[34]. The MatPIV package has been used to extract the velocity field, vorticity field, and flow streamlines in the system.

### 2.3 Model and simulations

We model this system by a continuum approach that we have recently developed[28] similar to previous models for flocking particles[35] or for active inelastic rods[36,37]. This model describes the

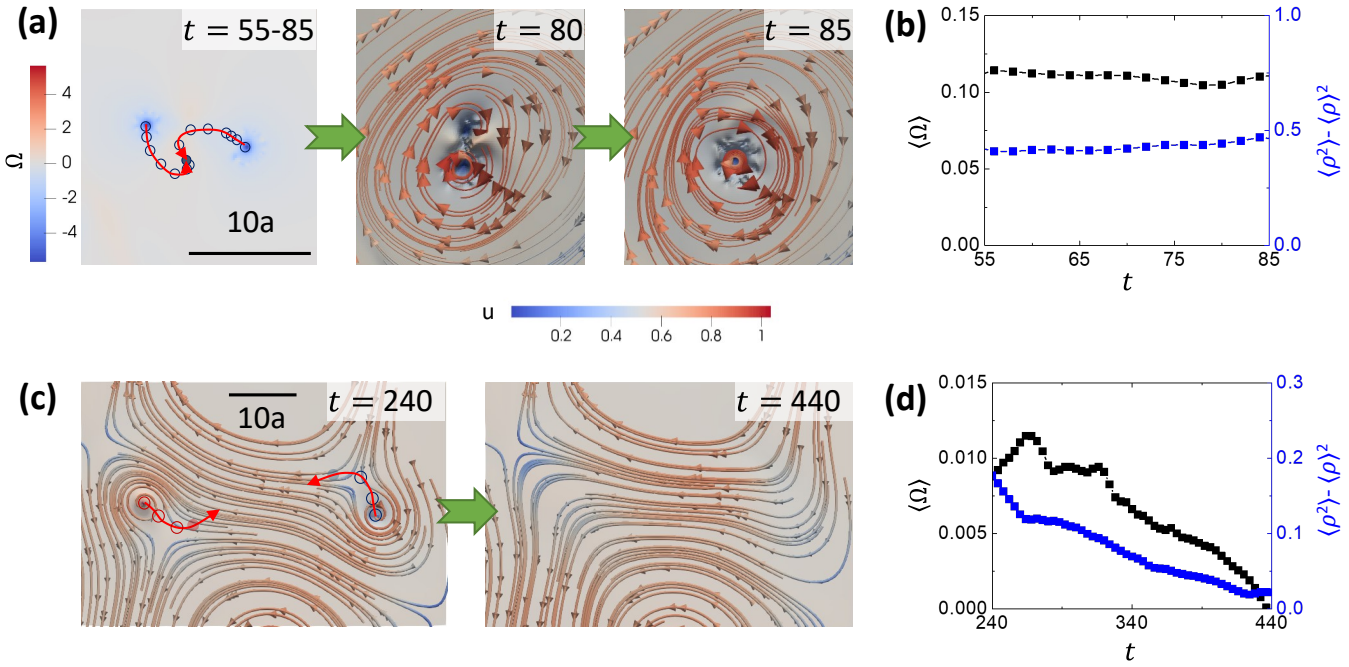


**Fig. 3** Recombination of two vortices in the early stages of an emerging multi-vortex state. **(a)** Process of merging two vortices with same chirality showing the vortex core trajectories and the final stages of the merging process as vorticity maps with particle velocity streamlines (see also Movie S4). The shown pair is highlighted in Fig. 4e). **(b)** Mean vorticity and variance of the particle density in the region shown in the left panels of (a). The particle variance does not change significantly over time, whereas the vorticity is slightly decreasing just before the merge as a result of the opposing motion of particle in the inter-vortex region. **(c)** Process of annihilation between two vortices with opposite chirality along with vortex core trajectories as long as detectable (see also Movie S5). **(d)** Mean vorticity and variance of the particle density in the region shown in (b). Due to the complete annihilation of the two vortices, both the mean vorticity and density variance decrease to zero.

dynamics of the system in terms of the coarse-grained roller velocity, $\mathbf{u}$, the depth-averaged fluid velocity, $\bar{\mathbf{v}}$, magnetic moment density, $\mu$, and number density of the rollers, $\rho$, as well as the coupling between the active rollers and the host fluid. Here we assume a shallow solvent, i.e., $|\nabla \mathbf{u}| \ll u/h$ and $|\nabla \rho| \ll \rho/h$, which described by the two-dimensional depth-averaged Navier-Stokes equation[38]. The dynamic equation for the particle velocity is a Ginzburg-Landay type equation with coupling to the hydrodynamics, as is the equation for the magnetic moment which includes a Landau-Lifshitz equation type damping, ensuring the alignment of the magnetization with the direction of the particle motion. In contrast to the previously used model, we also included a magnetic pressure term $p_\mu$, which accounts for the response to a magnetic field amplitude change and is a part of the magnetic stress tensor. The complete set of coupled partial differential equations describing the system dynamics is given by

$$\partial_t \mathbf{u} = \alpha \mathbf{u} - \beta |\mathbf{u}|^2 \mathbf{u} + D\nabla^2 \mathbf{u} + \frac{\nabla \cdot \Pi}{\rho m_0} + \gamma \rho \bar{\mathbf{v}} + \boldsymbol{\Omega}_{\mathrm{fl}} \times \mathbf{u}, \quad (1a)$$

$$\partial_t \bar{\mathbf{v}} = -(\bar{\mathbf{v}} \cdot \nabla)\bar{\mathbf{v}} - g\nabla h + \nu \nabla^2 \bar{\mathbf{v}} - \frac{3\nu}{h^2}\bar{\mathbf{v}} + \frac{\kappa \rho}{h^2}\mathbf{u}, \quad (1b)$$

$$\partial_t \boldsymbol{\mu} = \alpha \boldsymbol{\mu} - \beta' |\boldsymbol{\mu}|^2 \boldsymbol{\mu} + D\nabla^2 \boldsymbol{\mu} - \varepsilon \boldsymbol{\mu} \times [\boldsymbol{\mu} \times \mathbf{u}], \quad (1c)$$

$$0 = \partial_t \rho + \nabla \cdot \rho \mathbf{u}, \quad (1d)$$

$$0 = \partial_t h + \nabla \cdot h \bar{\mathbf{v}}, \quad (1e)$$

where $\boldsymbol{\Omega}_{\mathrm{fl}} = \frac{1}{2}\nabla \times \bar{\mathbf{v}}$ is the vorticity of the fluid, $g$ is the gravitational acceleration, $\nu$ the kinematic viscosity of the host fluid, $a_0$ the radius of a single roller, $\alpha = \tau_{\mathrm{col}}^{-1} - \tau_{\mathrm{dif}}^{-1}$ and $\beta' = \left(\rho^2 d_0^2 \tau_{\mathrm{col}}\right)^{-1}$ with $d_0$ being the magnetic moment of a single roller. $D$ is the translational diffusion coefficient, $D = \omega_0^2 d_0^2 \tau_{\mathrm{dif}}/4$ for self-propelled particles,and $\gamma = \frac{3}{4}\frac{a_0}{h}\tau_{\mathrm{col}}^{-1}$ is a numerical prefactor for the depth averaged in-plane velocity[28]. Important is the stress tensor $\Pi = -p\mathsf{I} + \mathsf{M}$, which accounts for, both, steric and magnetic interactions between rollers ($\mathsf{I}$ is the identity tensor). The first term, quantified by the pressure $p$ only contributes when particle start to overlap. The magnetic stress, $\mathsf{M}$, is a mean-field approximation of the magnetic interactions between rotating ferromagnetic moments in the continuum limit derived in detail previously in Ref.[28]. This tensor describes time averaged magnetic interactions between rotating moments in two dimensions. It also now includes a magnetic pressure term[33], $p_\mu \propto {H_0}^2 \rho$, to explicitly account for the influence of the external magnetic field amplitude. This procedure is justified by the fact that in the experiments a magnetic moment per roller is a combination of ferromagnetic component (rotating with the particle) and induced paramagnetic contribution (always along z direction) accounted now by the additional magnetic pressure term. The last two equations, (1d) and (1e), for the particle density, $\rho$, and fluid surface height, $h$, ensure the continuity of the model. As magnetic rollers constantly depart away (and subsequently return) from the interface due to non-negligible lift forces[30], we use a bulk value for the rotational drag coefficient in our model.

The formation of collective dynamic states in our system is a consequence of the competition between velocity alignments due to inter-particle collisions and, on the other hand, rotational diffusion, which homogenizes the system. This interplay is a source of instability captured by the model. In terms of the dynamical equation for the particle velocities, which is of Ginzburg-Landau type, this instability is directly reflected in the linear coefficient $\alpha$ being the difference of inverse mean collision time and inverse diffusion time. When the diffusion time is short, this linear coefficient could be negative resulting in a stable homogeneous (gaseous) solution. With decreasing collision time $\alpha$ becomes positive leading to collective dynamics. The model developed in our previous publication [28] captures a number of collective phases (flocks, vortices, traveling bands) reported in the corresponding phase diagram plotted as a function of average particle density and field frequency (controlling the activity of the rollers) [28].

These coupled equations are discretized on a regular mesh with periodic boundary conditions and numerically integrated in time on GPUs using a quasi-spectral split-step method, which evaluates all Laplacian terms in Fourier space. The typical mesh size is chosen as $a_0/8$ (i.e., the simulated system meshes are up to a size of $2048^2$) and the time step as $1/1500$ of a field cycle. To avoid a metastable homogeneous solution, we initialize the numerical model with random magnetization and velocity vector fields. The equation system is then integrated for about $4 \cdot 10^6$ time steps, which corresponds to about one minute at 40 Hz.

## 3 Results and discussion

In this paper, we delve into the vortex emergence and interaction dynamics at different length scales by complementing simulations (Fig. 1a) and experiments (Fig. 1b-d). Since the theoretical model is based on a coarse-grained continuum approximation capturing the system dynamics on length scales larger than the particle diameters, the flow pattern around individual rollers cannot be captured. However, the simulation system provides an insight into the large-scale dynamics. For instance, Fig. 1a gives an overview of an early state of the system before the formation of a steady multi-vortex state. The panel shows the vorticity $\Omega = \partial_x u_y - \partial_y u_x$ of the particle velocity as isosurface with superimposed flow-lines of the fluid (the full evolution is shown in Movies S1 & S2). In the case of the experimental system we have access to the dynamics of individual rollers. We utilize particle image velocimetry (PIV) to get an insight into the flow dynamics associated with individual rollers, and its role in the emergence of long-range orientational ordering in the ensemble. Fig. 1b and c shows a typical profile of the hydrodynamic flows generated by a single roller, which agrees well with the simulation result based on the smoothed particle hydrodynamics method [30]. The extracted velocity (Fig. 1b) and vorticity (Fig. 1c) maps along with the flow streamlines show the dipolar flow field. The circulating vortical flows promote specific interactions with the neighbouring rollers: neighbouring particles are pushed out at the front (with respect to the rolling direction) by repelling flows and can be pulled towards the back by the attracting flows while aligning the rollers velocities to each other. To characterize the roller-to-roller orientational alignment, we calculate the spatial velocity correlation, $C(\boldsymbol{r})$, between two rollers separated by a vector $\boldsymbol{r} = (r, \theta)$:

$$C(\boldsymbol{r}) = \left\langle \frac{u(\boldsymbol{r'},t) \cdot u(\boldsymbol{r'}+\boldsymbol{r},t)}{|u(\boldsymbol{r'},t)|^2} \right\rangle_{r',t} \quad (2)$$

Here, $u$ is the roller velocity, $\boldsymbol{r'}$ is the position of the reference roller, and $t$ is time. The velocity correlation map extracted from a flock of rollers shows that the rollers are coherently chasing each other on length-scales 200 $\mu$m $< r <$ 400 $\mu$m (Fig. 1d). These roller-induced hydrodynamic flows lead to self-alignment of neighboring rollers when they approach each other. Notably, this arrangement in the flock of rollers is similar to the pattern of stripes along the diagonals induced by the interaction of hydrodynamic dipoles [39–41].

### 3.1 Formation of seed vortices and their recombination

The formation of a multi-vortex state proceeds through the emergence of (seed) vortices from individual groups of rollers. Fig. 2a and Movie S3 illustrate the dynamics of a vortex self-organization from a larger group of rollers. For the sake of clarity, we visualize the moving direction of each roller by an arrow with angular-resolved color-coding, and overlay it with the flow streamlines. Initially, a group of rollers coupled by hydrodynamic flows induces local particle-number densifications flows that turn into flocks ($t_1$). The flocks form several transient vortices ($t_2$) of the same chirality that eventually merge into a single stable vortex ($t_3$).

This trend also correlates with the time evolution of the mean vorticity, $\langle\Omega\rangle$ , see Fig. 2b, which was averaged inside the dashed square area indicated in Fig. 2c). Our simulations yield a similar results. Fig. 2d shows in analogy with panel (b) the mean vorticity and also density variance averaged over a small region of the system shown in panel (e). Here, the density variance is the change of the particle density, $\rho$, with time starting from a slightly randomized homogeneous state. The change of the average vorticity in this region reflects, as the experiment, the evolution of small transient vortices with identical chirality into a larger, more stable vortex. This evolution event is also confirmed by a decrease of the particle density variance after reaching a maximum (corresponding to transient vortices) before the final merge.

The simulations also correctly capture the intermediate phase in which emergent seed vortices with random chirality evolve into sparse and isolated larger vortices with opposite chirality. To investigate the dynamics in this intermediate recombination phase, we looked at a pair of seed vortices (i) with identical chirality and (ii) with opposite chirality. Similar to the emergence phase, vortices with same chirality merge if they are close by, as shown in Fig. 3a and Movie S4. The analysis of the vorticity and density variance averaged over this small region reveals that they do not change much and remain almost constant during the merge process as seen in Fig. 3b. In the case (ii), which is much rarer compared to the case (i), it can happen that two seed vortices with opposite chirality annihilate each other only if they are close enough and confined by the surrounding stable vortices (Fig. 3c

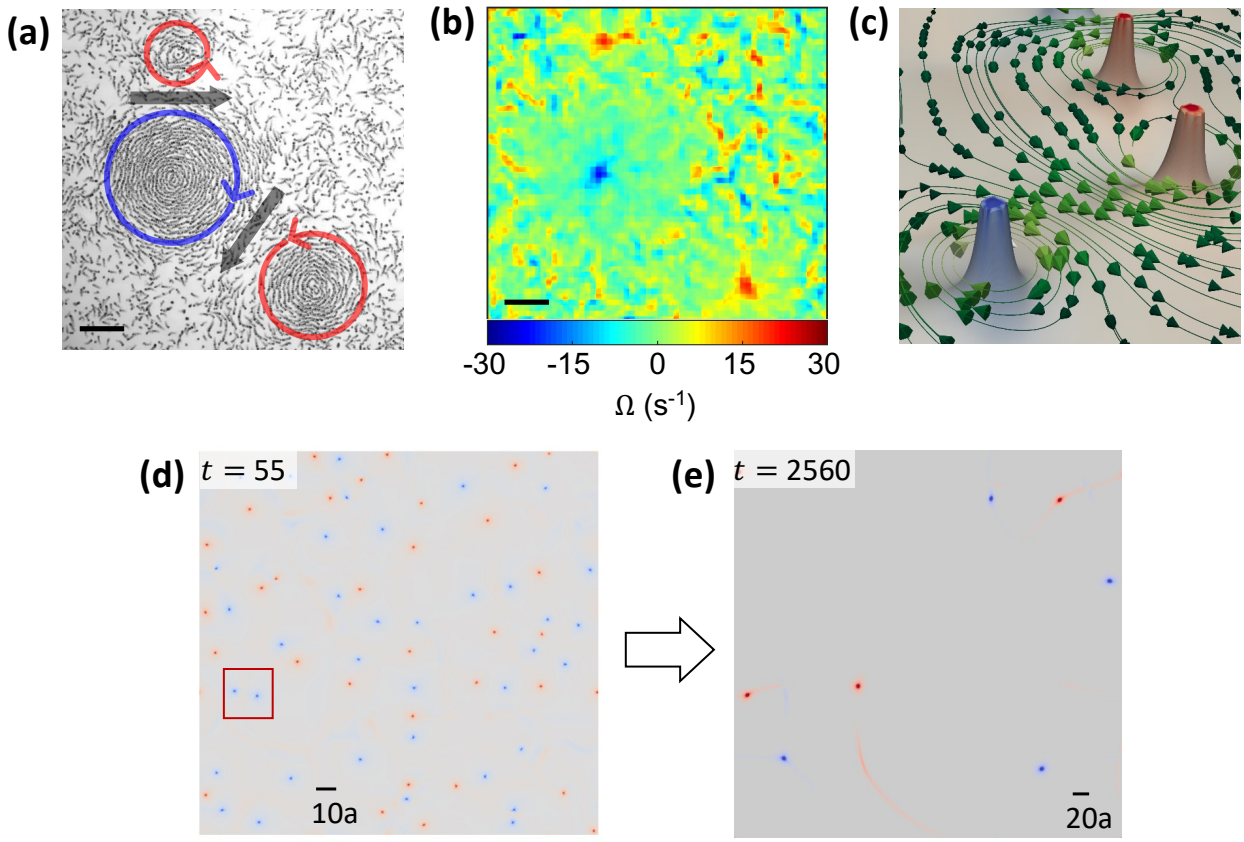


**Fig. 4** Multi-vortex state with opposite chirality (**a**) An overlay of five consecutive images representing a multi-vortex state with opposite chirality: a primary vortex with the left-handed chirality (blue) and secondary vortices with the right-handed chirality (red). The black arrows indicate the flow of the rollers moving in a coherent direction in-between neighboring vortices with opposite chirality. (**b**) The vorticity field of the rollers in the multi-vortex state, proving the opposite chirality of the neighboring vortices. The scale bars are 3 mm. (**c**) Close-up of a three-vortex region, where the particle density is shown as iso-surface, but colored by the vorticity (same as in Fig. 3), and particle velocities are shown as streamlines. Similar to the experimental result (a), the opposite chirality of the neighboring vortices facilitates the same directional fluid flows. (**d**) Vorticity field of a $128a \times 128a$ simulated system at an early time. The red box shows a pair of vortices with same chirality which are about to merge - shown in Fig. 3a). (**e**) Vorticity field of a larger $256a \times 256a$ simulated system at a late time emerged from the recombination of seed vortices in (d). The resultant vortices are quite stable and their recombination is rare where the neighboring vortices display opposite chirality.

and Movie S5). The averaged vorticity in the region of the annihilation event (Fig. 3d) is, as expected, relatively small, indicating that the magnitude of the vorticity of both vortices is comparable. The density variance also drops to zero in this region, leaving a homogeneous area behind.

After the recombination of seed vortices, the resultant stable vortices in the steady state favor the nearest neighborhood to be populated by vortices with opposite chirality, see Fig. 4a-c and Movie S6. Naturally, vortex-driven flows may promote the dynamic alignment and subsequent densifications of neighboring rollers giving rise to secondary neighboring vortices with opposite chirality. In Fig. 4a and 4b, the primary reference vortex has the clockwise (CW) chirality while the secondary vortices induced by the macroscopic flows from the reference vortex have the counter-clockwise (CCW) chirality. The opposite chirality of neighboring vortices facilitates unobstructed flows of rollers in-between vortices and thus is desirable to sustain a steady state of multiple vortices. The result is also captured in the simulations, see Fig. 4d). The simulations allow to resolve in detail the development of a global steady state in unconfined environment populated by multiple vortices with the preference of a quasi-antiferromagnetic ordering between them. Similar to experimental observations, the spontaneous local self-densification evolves into seed vortices that coalesce or annihilate with neighbors, eventually reaching a steady state formed by stable vortices. ( Fig. 4e→f)

Hydrodynamic interactions play a pivotal role in the emergence and stabilization of the multi-vortical states in ferromagnetic rollers ensembles. However, magnetic interactions are not negligible in the system and play an essential role affecting the short-range ordering between rollers in collective phases (such as vortices).

### 3.2 Magnetic field response and manipulation of self-organized multi-vortex states

The amplitude of the external magnetic field is a convenient knob to fine-tune the balance between hydrodynamic and magnetic interactions. We note that the change in the field amplitude neither alters the dynamics of individual rollers nor the roller-induced hydrodynamic flows because the rotation of the Ni spheres (re-

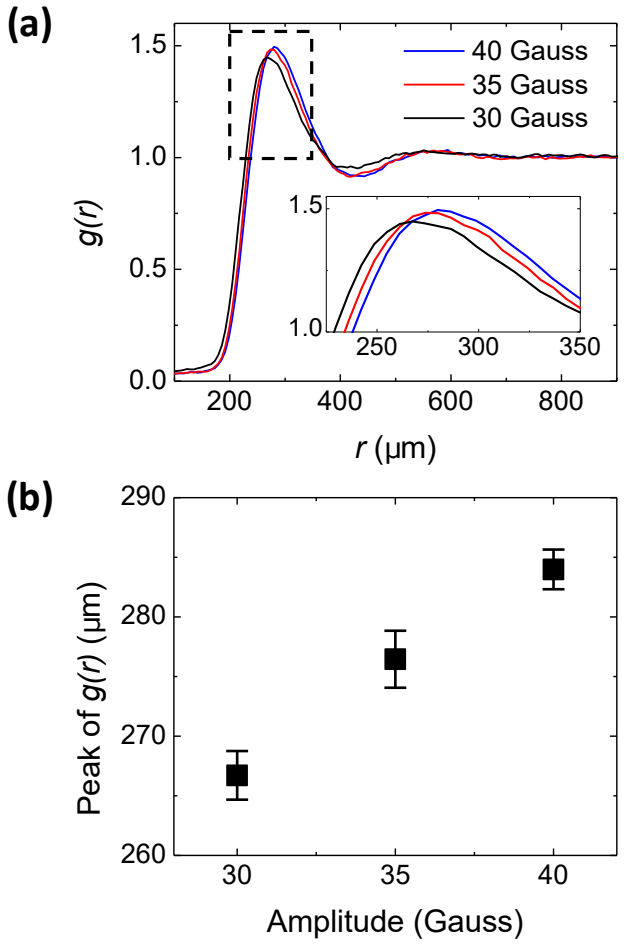


**Fig. 5** Roller-to-roller spacing in self-organized vortex state as a function of the amplitude of the driving magnetic field . (**a**) Radial distribution function of the rollers obtained for $H_0$ = 30G, 35G, and 40G. Inset: magnified area indicated by a dashed rectangle of the first peak position of g(r). (**b**) Evolution of the first peak position of g(r) with amplitude of the driving magnetic field.

sulting in activity) is synchronized with the magnetic field[17] and is fixed at $f = 40$ Hz in our current study. Instead, the field amplitude can independently tune the magnetic dipole-dipole interactions between the rollers. To prevent demagnetization of the Ni ferromagnetic particles only small variations of the field amplitude ($\delta H_0 = \pm 5G$) have been used. These field variations are not sufficient to change ferromagnetic moment of the particles (by the internal motion of magnetic domain walls in each particle) and changes only the induced paramagnetic moment of the particles. Since external driving magnetic field is always in $z$-direction, the induced paramagnetic moment contributes only to repulsive dipole-dipole interactions between the rollers. As a result, changes in the driving field amplitude are reflected in an increase of the typical roller-to-roller spacing inside vortices with the growth of the field amplitude, see Fig. 5.

The remaining question is, how variations on the microscale roller-to-roller spacing induced by the changes of the field amplitude affect the macroscale dynamics of the system. In our experiments we approach this question by observing changes in the macroscopic behavior of the system in response to small changes of the field amplitude ($\delta H_0 = \pm 5G$) relative to the reference field amplitude $H_0 = 35G$. Since the dynamical equations for our model do not include an explicit time-dependent magnetic field, we simulate the amplitude change by varying the magnetic pressure term, $p_\mu \propto H_0$, with respect to a reference value ($p_\mu = 0.5$) by $\delta p_\mu = \pm 0.25$. The "magnetic pressure" term counteracts gradients in the rollers number density, and results in the suppression (smoothing) of self-induced densifications corresponding to the vortices.

A typical response of the multi vortical state to changes of the magnetic field amplitude $H_0$ is shown in the Fig. 6. Overall, an increase of the field amplitude leads to a growth of the typical vortex size and a decrease of the rollers number density inside of each vortex. Here, to determine the vortex size, we use a similar procedure as in Ref.[10] and define the radius of the vortex core as the characteristic distance from the vortex center where the azimuthally averaged tangential velocity of the rollers reaches maximum. Lower field amplitudes lead to weaker magnetic dipole-dipole repulsions and result in shorter inter-roller distances in the vortices. Correspondingly, the local roller number density increases, see Fig. 6a. Lowering the field beyond 30 G in our system leads to the loss of the steady rotation of the magnetic particles and their subsequent aggregation. Conversely, higher magnetic driving field amplitudes promote stronger magnetic repulsion between the rollers, reducing the local particle number density in the vortex, and as a result produce larger vortices (Fig. 6c). The histogram of typical vortex sizes depending on the magnetic field amplitude is provided in Supplementary Fig. S1. Movie S7 demonstrates the dynamic response of a multi-vortex state to *in-situ* variations of the field amplitude (30→35→40 G).

Our simulations yield a similar field-amplitude-dependent dynamic response, but better capture the distribution of the local density on a larger scale based on the continuum approximation (Fig. 6d-f). The simulations visualize a clear transition of the peak local density in the core of emergent vortices with the change of the field amplitude.

## 4 Conclusions

In summary, we combine experiments and simulations to probe the underlying dynamics of active magnetic micro-rollers that result in the emergence of unconfined macroscopic vortices. Roller-induced hydrodynamic flows promote velocity alignment interactions and self-densifications in the ensemble of rollers that lead to the emergence of seed vortices. Those eventually evolve through aggregation and annihilation towards steady large-scale vortex structures. Macroscopic flows facilitated by self-organized vortices further promote the formation of neighboring vortices with opposite chirality states. We have demonstrated the control of local roller densities and vortex sizes in the multi-vortical state by fine-tuning the magnetic dipole-dipole interactions between the rollers through amplitude variations of the driving magnetic field. Our findings provide insights into the dynamics of collective macroscopic behavior of active roller suspensions from the perspective of their microscopic dynamics and parameters of the energizing field. We expect that similar principles could be ex-

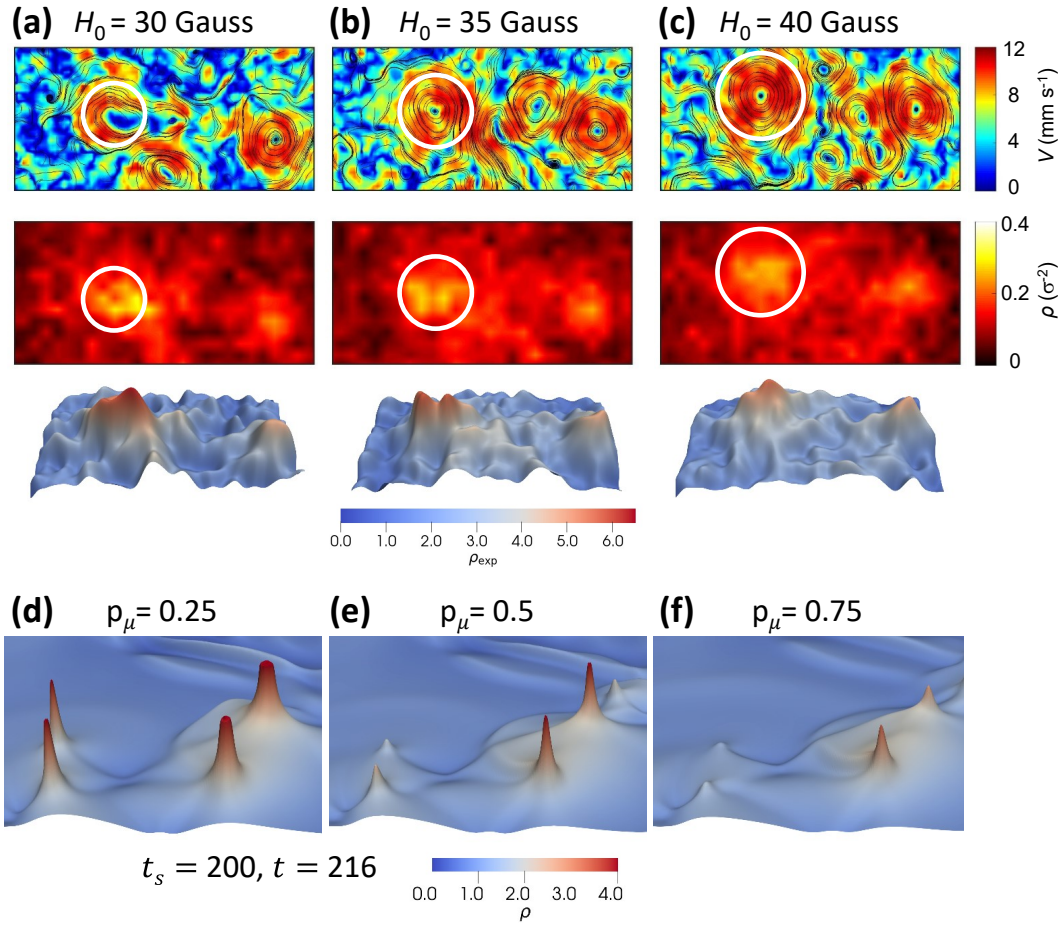


**Fig. 6** Response of the multi-vortex to magnetic field amplitude changes. Experimental: Panels (**a**)-(**c**) show the velocity field (top), 2D local density map (middle), and 3D local density map (bottom) depending on the field amplitude. White circles in the velocity field and 2D local density map indicate the location and sizes of the vortices. The vortex size increases and the local density decreases with an increase of the field amplitude. Simulations: Panels (**d**)-(**f**) show the particle density at time $t = 216$ after a change of magnetic pressure, $p_\mu$, mimicking the external field (see text) at time $t_s = 200$, at which the states were identical. (e) shows the unchanged reference state at $p_\mu = 0.5$. Upon decreasing $p_\mu$ to $0.25$, the maximum particle density and vorticity of the vortices goes up (in the shown window $\rho$ increases by about 3% and the vorticity by about 10%). When increasing $p_\mu$ to $0.75$, the maximum particle density and vorticity go down (here 17% and 20%, respectively).

tended to other active matter systems of torque-driven particles such as Quincke rollers and particles energized by rotating fields.

## Conflicts of interest

There are no conflicts to declare.

## Acknowledgements

The research was supported by the U.S. Department of Energy, Office of Science, Basic Energy Sciences, Materials Sciences and Engineering Division.

## Notes and references

1 T. Vicsek and A. Zafeiris, *Physics Reports*, 2012, **517**, 71.
2 M. C. Marchetti, J.-F. Joanny, S. Ramaswamy, T. B. Liverpool, J. Prost, M. Rao and R. A. Simha, *Reviews of Modern Physics*, 2013, **85**, 1143.
3 A. Cavagna, A. Cimarelli, I. Giardina, G. Parisi, R. Santagati, F. Stefanini and M. Viale, *Proceedings of the National Academy of Sciences*, 2010, **107**, 11865.
4 Y. Katz, K. Tunstrøm, C. C. Ioannou, C. Huepe and I. D. Couzin, *Proceedings of the National Academy of Sciences*, 2011, **108**, 18720.
5 A. Sokolov and I. S. Aranson, *Physical review letters*, 2012, **109**, 248109.
6 H. Wioland, F. G. Woodhouse, J. Dunkel, J. O. Kessler and R. E. Goldstein, *Physical Review Letters*, 2013, **110**, 268102.
7 I. H. Riedel, K. Kruse and J. Howard, *Science*, 2005, **309**, 300.
8 Y. Sumino, K. H. Nagai, Y. Shitaka, D. Tanaka, K. Yoshikawa, H. Chaté and K. Oiwa, *Nature*, 2012, **483**, 448.
9 A. Bricard, J.-B. Caussin, D. Das, C. Savoie, V. Chikkadi, K. Shitara, O. Chepizhko, F. Peruani, D. Saintillan and D. Bartolo, *Nature Communications*, 2015, **6**, 7470.
10 G. Kokot and A. Snezhko, *Nature Communications*, 2018, **9**, 2344.
11 S. Hernàndez-Navarro, P. Tierno, J. A. Farrera, J. Ignés-

Mullol and F. Sagués, *Angewandte Chemie International Edition*, 2014, **53**, 10696–10700.
12 B. Zhang, B. Hilton, C. Short, A. Souslov and A. Snezhko, *Physical Review Research*, 2020, **2**, 043225.
13 E. Lushi, H. Wioland and R. E. Goldstein, *Proceedings of the National Academy of Sciences*, 2014, **111**, 9733.
14 H. Wioland, F. G. Woodhouse, J. Dunkel and R. E. Goldstein, *Nature Physics*, 2016, **12**, 341.
15 K. Beppu, Z. Izri, J. Gohya, K. Eto, M. Ichikawa and Y. T. Maeda, *Soft Matter*, 2017, **13**, 5038.
16 D. Nishiguchi, I. S. Aranson, A. Snezhko and A. Sokolov, *Nature Communications*, 2018, **9**, 4486.
17 A. Kaiser, A. Snezhko and I. S. Aranson, *Science Advances*, 2017, **3**, e1601469.
18 H. Karani, G. E. Pradillo and P. M. Vlahovska, *Physical Review Letters*, 2019, **123**, 208002.
19 B. Zhang, A. Sokolov and A. Snezhko, *Nature communications*, 2020, **11**, 1–9.
20 B. Zhang, H. Karani, P. M. Vlahovska and A. Snezhko, *Soft Matter*, 2021, **17**, 4818–4825.
21 A. Snezhko, *Journal of Physics: Condensed Matter*, 2011, **23**, 153101.
22 Z. Lin, C. Gao, M. Chen, X. Lin and Q. He, *Current Opinion in Colloid & Interface Science*, 2018, **35**, 51–58.
23 M. Driscoll and B. Delmotte, *Current Opinion in Colloid & Interface Science*, 2019, **40**, 42.
24 K. J. Solis and J. E. Martin, *Soft matter*, 2017, **13**, 5676–5683.
25 P. Tierno and A. Snezhko, *ChemNanoMat*, 2021, **7**, 1–14.
26 J. E. Martin and A. Snezhko, *Reports on Progress in Physics*, 2013, **76**, 126601.
27 V. Soni, E. S. Bililign, S. Magkiriadou, S. Sacanna, D. Bartolo, M. J. Shelley and W. T. Irvine, *Nature Physics*, 2019, **15**, 1188.
28 K. Han, G. Kokot, O. Tovkach, A. Glatz, I. S. Aranson and A. Snezhko, *Proceedings of the National Academy of Sciences*, 2020, **117**, 9706–9711.
29 K. Han and A. Snezhko, *Lab on a Chip*, 2021, **21**, 215–222.
30 Y. Wang, S. Canic, G. Kokot, A. Snezhko and I. Aranson, *Physical Review Fluids*, 2019, **4**, 013701.
31 P. Tierno, R. Golestanian, I. Pagonabarraga and F. Sagués, *Physical Review Letters*, 2008, **101**, 218304.
32 S. Kim and S. J. Karrila, *Microhydrodynamics: Principles and Selected Applications*, Courier Corporation, 2013.
33 T. Mohoric, G. Kokot, N. Osterman, A. Snezhko, A. Vilfan, D. Babic and J. Dobnikar, *Langmuir*, 2016, **32**, 5094–5101.
34 J. C. Crocker and D. G. Grier, *Current Opinion in Colloid & Interface Science*, 1996, **179**, 298.
35 J. Toner and Y. Tu, *Physical Review E*, 1998, **58**, 4828.
36 I. S. Aranson and L. S. Tsimring, *Physical Review E*, 2005, **71**, 050901.
37 I. S. Aranson and L. S. Tsimring, *Physical Review E*, 2006, **74**, 031915.
38 A. Constantin and J. Escher, *Acta Mathematica*, 1998, **181**, 229–243.
39 T. Beatus, R. H. Bar-Ziv and T. Tlusty, *Physics reports*, 2012, **516**, 103–145.
40 I. Shani, T. Beatus, R. H. Bar-Ziv and T. Tlusty, *Nature Physics*, 2014, **10**, 140–144.
41 T. Beatus, I. Shani, R. H. Bar-Ziv and T. Tlusty, *Chemical Society Reviews*, 2017, **46**, 5620–5646.